



LAWRENCE  
LIVERMORE  
NATIONAL  
LABORATORY

# High strain-rate plastic flow in Fe and Al

R. F. Smith, J. E. Eggert, R. E. Rudd, C. A. Bolme, G. W. Collins

May 17, 2011

Journal of Applied Physics

## **Disclaimer**

---

This document was prepared as an account of work sponsored by an agency of the United States government. Neither the United States government nor Lawrence Livermore National Security, LLC, nor any of their employees makes any warranty, expressed or implied, or assumes any legal liability or responsibility for the accuracy, completeness, or usefulness of any information, apparatus, product, or process disclosed, or represents that its use would not infringe privately owned rights. Reference herein to any specific commercial product, process, or service by trade name, trademark, manufacturer, or otherwise does not necessarily constitute or imply its endorsement, recommendation, or favoring by the United States government or Lawrence Livermore National Security, LLC. The views and opinions of authors expressed herein do not necessarily state or reflect those of the United States government or Lawrence Livermore National Security, LLC, and shall not be used for advertising or product endorsement purposes.

# High strain-rate plastic flow in Fe and Al

R.F. Smith<sup>1</sup>, J.E. Eggert<sup>1</sup>, R.E. Rudd<sup>1</sup>, C.A. Bolme<sup>2</sup>, G.W. Collins<sup>1</sup>

<sup>1</sup>*Lawrence Livermore National Laboratory, P.O. Box 808, Livermore, CA 94550, USA*

<sup>2</sup>*Los Alamos National Laboratory, P.O. Box 1663, Los Alamos, NM 87545, USA*

Thin Fe and Al foils were ramp compressed over several to tens of ns timescales to study the time-dependence associated with the onset of plastic flow. Peak stress states of 15-200 GPa were achieved through a laser ramp-compression technique in which the strain rate can be varied, shot-to-shot, in the  $10^6$ - $10^8$  s<sup>-1</sup> range. In our analysis we find, a strong correlation between the peak elastic precursor stress,  $\sigma_E$ , and the strain rate at the onset of plastic flow,  $\dot{\epsilon}^p$ . Our data, combined with data from other dynamic compression platforms, reveal a sharp increase in  $\sigma_E$  at high strain rates, consistent with a transition from dislocation flow dominated by thermal activation and athermal effects to a phonon drag regime. In bcc Fe, this change in deformation response occurs at  $\dot{\epsilon}^p \sim 2 \times 10^6$  s<sup>-1</sup> and  $\sigma_E \sim 1.3$  GPa. In fcc Al, phonon drag dominates above  $\dot{\epsilon}^p \sim 10^3$  s<sup>-1</sup> and  $\sigma_E \sim 0.03$  GPa where  $\sigma_E$  scales as  $(\dot{\epsilon}^p)^{0.43}$ . By contrast, the Al alloy 6061-T6 exhibits a relatively weak dependency of  $\sigma_E$  with  $\dot{\epsilon}^p$  up to strain rates of  $\sim 10^7$  s<sup>-1</sup>.

## I. Introduction

Understanding the nature and time-dependence of material deformation at high strain rates is an important goal in condensed matter physics. Under dynamic loading, the rate of plastic strain,  $\dot{\epsilon}$ , is determined by the flow of dislocations and is a complex function of time, sample purity, temperature, internal stresses, microstructure and loading rate. Deformation at high strain rates is typically characterized in split-Hopkinson pressure bar ( $\dot{\epsilon} < \sim 5 \times 10^5 \text{ s}^{-1}$ ) or in shock compression ( $\dot{\epsilon} < \sim 10^6 \text{ s}^{-1}$ ) experiments where, for a known input, the bulk response of a sample is evaluated through analysis of transmitted wave profiles. For low stress shocks, an elastic wave emerges with a time-dependent stress,  $\sigma_E$ , which runs ahead of the plastic wave. Time-dependent plasticity is typically inferred in shock experiments by fitting measured  $\sigma_E$ -distance data with a phenomenological dislocation kinetics model [1-3]. In this paper, we employ a laser-driven ramp wave loading (RWL) technique in which the strain rate of compression is variable in the  $\sim 10^6$ - $10^8 \text{ s}^{-1}$  range. Our data shows that independent of sample thickness,  $\sigma_E$ , is well correlated with the instantaneous strain rate at the onset of plastic flow,  $\dot{\epsilon}$  for both shock- and ramp-wave experiments. At low strain rates  $\sigma_E$  increases linearly with  $\ln(\dot{\epsilon})$ ; characteristic of thermally-activated dislocation flow. At high strain rates there is a transition to a  $\sigma_E \propto (\dot{\epsilon})^n$  scaling consistent with phonon drag mediated dislocation flow.

The  $\sigma_E(\dot{\epsilon})$  onset for phonon drag dominated dislocation flow in bcc metals has not been observed experimentally. Recent measurements on bcc metals, V and Ta, using x-ray radiography to determine the growth of Rayleigh-Taylor instabilities inferred, via recourse to a multi-scale model, phonon drag mediated plasticity at  $\dot{\epsilon} \sim 10^7 \text{ s}^{-1}$  [4]. Similar experiments and analysis techniques, also on V and Ta, at  $\dot{\epsilon} \sim 10^5 \text{ s}^{-1}$  were consistent with plasticity in the thermal activation regime [5]. Kolsky bar experiments and pressure-shear experiments (tilted flyer plate impacts) on V up to strain rates of  $10^5 \text{ s}^{-1}$  [6] and Ta up to  $5 \times 10^5 \text{ s}^{-1}$  [7], have also been interpreted as falling in the thermal activation regime. Based on these limited data, for bcc metals, the dominant mechanism limiting plastic flow appears to be thermal activation up to  $\sim 5 \times 10^5 \text{ s}^{-1}$ , and phonon drag at  $10^7 \text{ s}^{-1}$  and above. Up until now there has not been a single technique that can vary the strain rate over a large enough interval in the correct high-rate regime to map out this transition. The new high- $\dot{\epsilon}$  data for bcc Fe presented in this paper is consistent



with high strain rate change to a phonon drag regime at  $\sigma_E \sim 1.3$  GPa and  $\dot{\epsilon} \sim 2 \times 10^6$  s<sup>-1</sup>. At higher strain rates  $\sigma_E$  scales linearly with  $\dot{\epsilon}$ .

In fcc metals, such as Al, the Peierls force is small and phonon drag is the dominant mechanism determining dislocation motion even at low  $\sigma_E(\dot{\epsilon})$ . We present new high strain rate ( $\sim 10^3$ - $10^{10}$  s<sup>-1</sup>) ramp and shock compression data on pure aluminum, which reveal that in the high- $\sigma$  phonon drag regime  $\sigma_E$  scales as  $(\dot{\epsilon})^{0.43}$ . We show that for a commonly used alloy of aluminum (Al 6061-T6) the high strain rate  $\sigma_E(\dot{\epsilon})$  data are consistent with a delayed onset of phonon drag mediated deformation due to impurities impeding dislocation flow. To our knowledge, the RWL data presented here represent the highest strain rate measurements on bcc and fcc metals reported to date.

## II. Experimental Setup

The RWL data reported here was obtained on the Janus and Omega laser facilities. The target design for the Janus experiments consists of a 100 $\mu$ m polyimide [C<sub>22</sub>H<sub>10</sub>N<sub>2</sub>O<sub>5</sub>] foil followed by a 200 $\mu$ m vacuum gap and an Fe/sapphire target (Fig. 1). The polyimide is irradiated for 4ns by the 1mm-square spatially-planar 527nm Janus laser (300 J), generating an ablatively-driven shock. After shock-breakout from the rear surface, the polyimide rarefies across the vacuum gap, monotonically loads-up against the Fe sample, and launches a temporally-smooth ramp-compression wave [10]. By changing the vacuum gap size and laser intensity it is possible to vary the compression rate by a factor of  $\sim 40$ . Under these conditions, peak stress states of 15-50 GPa are obtained over several to tens of ns. Due to the planar, inertially confined nature of the ramp drive our samples are in a state of uniaxial strain. Here, stress and strain are defined as  $\sigma = \sigma_{xx}$  and  $d\epsilon = d\rho/\rho$ . For the experiments on the Janus laser, high purity (99.995%) Fe was deposited in 10-36  $\mu$ m layers onto a sapphire [001] window under conditions that yielded a grain size of  $\sim 5$   $\mu$ m in the stress loading direction and  $\sim 1$   $\mu$ m in plane. The Fe bcc crystal structure was orientated along the [110] axis in the growth (pressure loading) direction with random orientation in-plane and was measured to be fully dense (7.87 g/cc) to within an accuracy of 0.6%. For the experiments on the Omega laser 12% Br-doped plastic foils [C<sub>4</sub>H<sub>3</sub>Br] were used instead of polyimide and the target was driven over a 2mm diameter by x-radiation from a Au hohlraum [11]. Here, 20-56  $\mu$ m thick single crystal [100] Fe samples were glued onto sapphire windows with an estimated glue thickness of  $\sim 1$   $\mu$ m. In both experimental setups, the time history of the transmitted compression wave was recorded by measuring the Fe/sapphire interface velocity  $u_i(t)$  with a line-imaging velocity interferometer system for any

reflector (VISAR) with a velocity accuracy of  $\sim 10$  m/s and a streak camera temporal resolution of  $\sim 0.05$  ns [12]. Sapphire was chosen because it has a similar mechanical impedance to Fe thereby minimizing wave reflections at the Fe-sapphire interface. For some experiments Fe/sapphire samples were replaced with Al/LiF samples. The high spatial planarity associated with the x-ray drive from the Omega laser meant different thicknesses of Al could be compressed with a common compression history to peak stress states of 200 GPa [13].

A typical  $u_i(t)$  profile for a ramp loaded polycrystalline Fe sample is shown in Fig. 1. Here, a three wave structure emerges at the Fe/sapphire interface: an elastic wave with a peak velocity of  $u_E$ , a plastic wave P1 with a peak velocity  $u_{\alpha \rightarrow \epsilon}$ , which is followed by a pronounced velocity pullback after the peak, and a subsequent plastic wave P2. This transformation from the smoothly rising load profile to the structured transmitted wave profile is understood by considering the target dynamics in Lagrangian coordinates as discussed in ref. [10]. The initial one-dimensional elastic deformation is characterized by stress propagation at the longitudinal sound speed ( $\sim 5.1$  km/s). Immediately behind the elastic front, as plasticity initiates, stress waves propagate at the lower bulk sound speed ( $\sim 4.4$  km/s) which results in wave separation as a function of thickness. For stress levels above 13 GPa the  $\alpha \rightarrow \epsilon$  (bcc  $\rightarrow$  hcp) phase transformation may initiate causing a drop in the Lagrangian sound speed,  $C_L$ , as the material evolves into the new  $\epsilon$ -phase. Due to the time-dependence associated with the transformation, at  $u_{\alpha \rightarrow \epsilon}$  there is a rapid velocity pullback in the  $u(t)$  record due to stress relaxation caused by an evolving volume collapse into the denser  $\epsilon$ -phase. The velocities associated with peak elastic stress and the onset of the  $\alpha \rightarrow \epsilon$  phase transformation have a strong dependence on the loading strain rate. Within this paper we focus solely on the time dependence associated with the initial onset of plasticity for bcc Fe and fcc Al. These results are presented in the following sections.

### III. Review of Experimental Data

#### A. bcc Iron

The velocity of the Fe/sapphire interface may be related to an equivalent longitudinal stress,  $\sigma_x$ , and particle velocity,  $u$ , with standard impedance matching techniques assuming an elastic EOS for sapphire ( $\sigma_x = 44.2u + 4.7u^2$  [14]) and, for compression below  $u_E$ , an elastic EOS for Fe ( $\sigma_x = 43.67u + 11.88u^2$  [15]) with  $\sigma_E$  and  $u$  in GPa and km/s, respectively. For compression above  $u_E$ , an EOS for  $\alpha$ -Fe was used,

which was determined from a fit to shock Hugoniot data reported by Arnold [16] ( $\sigma_{\alpha\text{-phase}}=0.25 +36.93u +6.78u^2$ ). In our analysis we define a longitudinal strain rate associated with initial plastic flow as,

$$\dot{\gamma} \equiv \frac{d \ln V}{dt} = \frac{du/dt}{C_L} \equiv \dot{\gamma} \Big|_{u_E}^{2u_E}, \quad (1)$$

where  $C_L$  is the Lagrangian sound speed. In the analysis presented below, is defined at the base of the P1 wave over the velocity interval  $u_E$  to  $2u_E$  (Fig 1) and represents the strain rate at the onset of inelastic deformation. Based on recent sound speed measurements on 99.8% pure Fe,  $C_L$  is assumed constant over this velocity interval at 4.4 km/s [17].

Shown in Fig. 2 is the peak longitudinal elastic stress plotted as a function of sample thickness, for our laser RWL data and those previously published from other dynamic compression experiments (both ramp and shock). For each data set used, the reported initial microstructures and sample purities from the original references are listed. The error bars for the Janus laser ramp data (red circles) on polycrystalline Fe represent the uncertainty in the determination of  $u_E$  due to instrument resolution and non-planarities within the drive. For comparable loading drives on the Omega laser, the [100] single crystal Fe samples (purple open diamond symbols) exhibit  $\sigma_E$  up to five times greater than the equivalent measurement on polycrystalline samples. This trend is consistent with observations by Jensen [18] in which  $\sigma_E(500\mu\text{m})$  for [100] single crystal Fe was greater by a factor of  $\sim 2$  over similar measurements on polycrystalline samples. In the same study  $\sigma_E(500\mu\text{m})$  was found to be comparable for polycrystalline Fe and Fe [210] and [110] single crystals, which suggests that the discrepancy in our data between polycrystalline and [100] is not due primarily to differences in the initial dislocation density but rather on the availability of slip planes to facilitate plasticity. In the Omega [100] data large velocity pullbacks were measured after the elastic precursor peak.  $\sigma_E(x)$  shown in Fig. 2 was calculated at the precursor peak and the extent of the (negative) error bar represents the position of the symbol if the minimum pullback velocity were used to calculate  $\sigma_E(x)$ . A similar analysis was applied to the shock compression data from Arnold [16, 19], Barker [20], Jensen [15], Hereil [21], Taylor [22] and Johnson [23] and to the ramp compression data from Jensen [18]. The  $\sigma_E(x)$  data of Bancroft [24], de Ressiguier [25], Ivanov [26] and Rosenberg [27] are listed as reported. In these references no  $u(t)$  profiles were given. The laser ramp compression data presented here represent the closest elastic stress measurements to the loading surface reported to date.

For polycrystalline Fe, there is a general trend of  $\sigma_E$  decay as a function of distance away from the loading surface ranging from 5.5 GPa at 10  $\mu\text{m}$  to 0.6 GPa at 133mm [24]. After sufficient

propagation,  $\sigma_E$  asymptotes toward the steady-state yield surface or Hugoniot Elastic Limit (HEL). For the Janus RWL loading data and for a fixed thickness of 20 $\mu\text{m}$ ,  $\sigma_E$  varies by a factor of  $\sim 3$ . A similar scatter is observed at 50 $\mu\text{m}$  for the [100] single crystal RWL data. The origin of this scatter may be understood by considering the effect of loading strain rate on the evolution of the peak elastic stress.

Figure 2 represents the *instantaneous* value for  $\sigma_E$  after propagation through a range of sample thicknesses; a data set which encompasses a wide range of loading rates. Figure 3(a) illustrates the time-dependent evolution of  $\sigma_E$  as a function of propagation distance from the loading surface, for shock compression (red dashed curve) and for ramp compression (black dashed curve) experiments. Under shock loading the material is brought to the compressed state within the rise time of the shock front ( $\sim 10$  ps). The initial deformation at the loading surface is assumed to be fully elastic and at a stress state given by the peak loading stress [1-3]. After a finite period, significant plastic flow behind the elastic front is initiated with an associated drop in the material sound speed. For moderate shock stresses, a two wave structure is formed with a predominantly elastic wave, travelling initially at the longitudinal sound speed, running ahead of a slower moving inelastic wave propagating at a stress-dependent bulk sound speed. Time-dependent plastic flow behind the elastic front causes the peak elastic precursor stress,  $\sigma_E$ , to decay as a function of propagation distance. Here, disturbances behind the elastic front with an associated sound speed,  $c$ , propagate in  $x$  with a velocity  $u + c$ , where  $u$  is the particle velocity behind the shock front. Attenuation of a shock front, propagating in  $x$ , by a release wave may be written as,

$$\frac{DP}{DX} = -\frac{(u+c-U)}{U} \frac{\partial p}{\partial x}, \quad (2)$$

where  $DP/DX$  refers to the attenuation of the peak,  $\delta p/\delta x$  refers to the change in slope behind the shock front and  $U$  is the velocity of the shock front [30, 31]. The difference  $(u+c)-U$  increases monotonically with the curvature of the Rankine-Hugoniot  $p$ - $v$  curve, so equation (2) shows that shock decay is rapid where the thermodynamic derivative  $\delta^2 p/\delta v^2$  is large in the shocked state and  $\delta p/\delta x$  is large, i.e. the shock is a sharp spike [31]. Consequently, close to the loading surface where stress relaxation behind the elastic front is strongest,  $\sigma_E$  decays most rapidly. A full description of precursor decay as given in equation (2) requires an understanding of the evolution of  $u(x)$  and  $c(x)$ , which implies a knowledge of time-dependent dislocation flow. At long distances a steady wave emerges with fixed amplitude elastic precursor at the Hugoniot Elastic Limit (HEL) and a plastic wave rise time determined by a competition between the nonlinear stress-strain response and dissipative behavior [28, 29].

While shock compression is characterized by a reduction in strain rate as a function of propagation distance towards a steady wave value, in ramp compression experiments the strain rate *increases* with distance from the loading surface towards an equivalent shock rise time (Fig. 3(a)). Unlike shock loading, for ramps  $\sigma_E(x=0)$  is not equivalent to the peak compressive stress but rather is a function of the interplay between loading rate and the time dependence of incipient plasticity. In order to investigate how the peak elastic stress in ramp compressed Fe is related to the kinetics of plastic flow, we apply a rate-dependent, dislocation-based continuum model of plasticity. A detailed description of this model may be found in Appendix A. Plotted in Fig. 3(b) is the calculated response of an Fe sample to dynamic loading where the peak state of compressive stress is constant but the loading rate is varied from  $10^6$ - $10^9 \text{ s}^{-1}$ . The resolved shear stress,  $\tau$ , versus time is derived by solving the differential equations describing a linear increase of applied shear stress with time and those describing time-dependent plasticity. As material flow is not considered, the calculations represent the onset of plasticity at the loading surface. This simple model shows that, at  $x=0$ ,  $\tau$  increases linearly with time until the material undergoes a transition from elastic to plastic deformation at  $\tau_E$ , where  $\tau_E$  is found to be uniquely related to the loading strain rate,  $\dot{\gamma}_{\text{Load}}$ . The onset of plasticity results in shear stress relaxation; initiated at  $\tau_E$ , and at a rate proportional to  $\tau_E$ . We note that a quantitative description of  $\sigma_E - \dot{\gamma}$  material response at a distance  $x'$  from the loading surface is highly complex and is a convolution of the instantaneous material response (Fig. 3(b)) and the integrated time-dependent response from  $x=0 \rightarrow x'$  (Fig. 3(a)).  $\dot{\gamma}(x')$  is determined by the flow of dislocations and is a complex function of time, sample purity, temperature, internal stresses, microstructure and loading rate. However our analysis shows a direct correlation between the peak elastic stress ( $\sigma_E$ ) and the strain rate at the onset of plastic flow ( $\dot{\gamma}$ ) at the loading surface. Away from the loading surface the attenuation of  $\sigma_E$  in  $x$  is also strongly correlated to time-dependent plastic flow ( $\dot{\gamma}$ ), through the  $\delta p / \delta x$  term in eqn. 2.

In Fig. 4, we plot the *instantaneous*  $\sigma_E - \dot{\gamma}$  response of Fe for a range of sample thicknesses. Only data sets from Fig. 2 where  $u(t)$  profiles were available are represented. For the shock compression data of Arnold [16, 19] and Hérelil [21] we use the strain rate numbers as reported. The shear stress measurements from Klopp [33] were converted to longitudinal stress and strain rate as described in ref. [34]. The data set taken as a whole represents a large range of initial Fe microstructures. The Janus RWL samples had  $\sim 1 \times 5 \text{ } \mu\text{m}$  grains while the work of Jensen [18] used single crystal Fe samples with different crystal orientations. Grain size dependences on  $\sigma_E - \dot{\gamma}$  data for Armco Fe in the  $5 \times 10^4 - 10^6 \text{ s}^{-1}$  strain rate range was first reported by Arnold [16] with subsequent analysis by Armstrong [19]. The strain rate

dependence of  $\sigma_E$  for different grain sizes, was accounted for in terms of competition between grain-size-dependent slip and twinning deformation responses followed by grain-size-independent shock-induced plasticity controlled by the nucleation of deformation twins [19, 25]. The lower  $\sigma_E$  value for the 400 $\mu\text{m}$  grain data from Arnold [16] is explained as a consequence of twinning being the dominant deformation mechanism as opposed to slip deformation for the 20, 40 and 80 $\mu\text{m}$  size grains [19].  $\sigma_E$  for the 400 $\mu\text{m}$  grain samples reported by Johnson [23] is significantly higher, but this discrepancy may be accounted for by the higher levels of impurities within these samples. The work by Arnold suggests that the  $\sigma_E$ - $\dot{\epsilon}$  response is insensitive to microstructure for grain size less than  $\sim 40\mu\text{m}$ .

The data in Fig. 4 shows a relative insensitivity of  $\sigma_E$  with strain rate for polycrystalline Fe over the strain rates range  $\sim 10^2$ - $10^6 \text{ s}^{-1}$ . At  $\dot{\epsilon} > \sim 2 \times 10^6 \text{ s}^{-1}$  there is a marked increase in  $\sigma_E$  scaling with  $\dot{\epsilon}$ . A number of phenomenological constitutive models have been developed to describe the  $\dot{\epsilon}$  relationship in bcc metals. A general form of these models predicts a  $\sigma \propto \ln(\dot{\epsilon})$  dependency in the thermally-activated regime with a transition to a  $\sigma \propto (\dot{\epsilon})^n$  response in the high strain rate phonon drag regime [8], where  $n < 1$  suggests an increase in saturation dislocation density with increasing strain rate [32]. A fit to the low strain rate data, shown as the black line in Fig. 4 is represented by the following expression,

$$\sigma_E = 0.06 \ln(1887 \dot{\epsilon}), \quad (3)$$

which is consistent with a thermally-activated dislocation flow facilitating the onset of significant plasticity. For  $\dot{\epsilon} > \sim 2 \times 10^6 \text{ s}^{-1}$ ,  $\sigma_E$  increases linearly with  $\dot{\epsilon}$ . This sudden change in material response is consistent with high- $\dot{\epsilon}$  predictions for bcc metals where dislocation velocities become limited only by energy dissipation from interaction with lattice vibrations or phonon drag [35]. A fit to the high strain rate data, shown as the green curve in Fig. 7, is represented by the following expression,

$$\sigma_E = 1.11 + 1.45 \times 10^{-7} \dot{\epsilon}. \quad (4)$$

The data in Fig. 4 are consistent with a change in the dislocation flow mechanism from thermally activated to phonon drag at  $\sigma_E$  of  $\sim 1.3 \text{ GPa}$  and  $\dot{\epsilon} \sim 2 \times 10^6 \text{ s}^{-1}$ . Additional measurements by Hérel [21] at a strain rate of  $\sim 10^6 \text{ s}^{-1}$  demonstrated a linear drop in  $\sigma_E$  as a function of increasing temperature; consistent with thermally activated dislocation flow and the conclusions reached here. Single crystal [100] Fe data is represented as the open diamond symbols. Here, the more limited data set suggests an equivalent transition to a phonon drag regime at  $\sim 10^6 \text{ s}^{-1}$  but offset to higher levels of  $\sigma_E$ .

Fig. 2 and 4 illustrates that for moderate strength shocks high strain rate plastic deformation exists only close to the loading surface. It would be expected, therefore, that (high- $\sigma_E$ ) phonon drag is initially the dominant mechanism limiting dislocation flow whereas after significant propagation and commensurate reductions in  $\sigma_E$ , thermal activation would predominate. Consequently, under shock compression, a measurement of  $\sigma_E$  versus  $\dot{\epsilon}$ , as a function of distance would reveal the  $\sigma_E$  state at which phonon drag initiates. In the ramp compression experiments reported here, an analogous experimental measurement is made. Here, for Fe, the target thickness is held fixed at 10-30  $\mu\text{m}$  and the strain rate is varied in the  $\sim 10^6$ - $10^7 \text{ s}^{-1}$  range.

In our analysis we correlate the peak elastic stress with the strain rate at the onset of plastic flow,  $\dot{\epsilon}$ . In the work of Swegle and Grady [28] it was found that, under steady wave conditions, the maximum strain rate within the plastic wave has a forth-power relationship to the peak shock stress,  $\dot{\epsilon}_{\text{max}} \propto \sigma_{\text{Peak}}^4$ . Remarkably, this relationship appears to be universal over all (fully dense) materials. The underlying physics of the 4<sup>th</sup> power law are not well understood and a number of physical mechanisms have been proposed [29]. There is evidence however that the physical processes defining  $\dot{\epsilon}_{\text{max}}$  and the low stress  $\dot{\epsilon}$  used here are different. As reported by Grady, a lower stress limit to the applicability of the 4<sup>th</sup> power law occurs when the peak flow stress approaches the yield stress. In recent work on Fe by Armstrong et al. [19] it was shown that the  $\dot{\epsilon}_{\text{max}}$  asymptotes towards the 4<sup>th</sup> power dependency only for flow stresses above  $\sim 8 \text{ GPa}$ . The low stress divergence from 4<sup>th</sup> power law behavior was accounted by Armstrong through a dislocation dynamics based model.

## B. fcc Aluminum

In fcc metals, such as Al, the Peierls force is small and phonon drag is the dominant mechanism determining dislocation motion even at low  $\sigma(\dot{\epsilon})$ . Shown in Fig. 5 is the peak longitudinal elastic stress in pure Al as a function of propagation distance,  $\sigma_E(x)$ , for our laser ramp wave data and those previously published from other dynamic compression experiments. For each data set used, the listed initial microstructures and sample purities are taken from the original references. The error bars for the data taken on the Janus laser represent the uncertainty in the determination of  $u_E$  due to instrumental resolution and non-planarities within the drive. Here, no velocity pullback associated with the elastic precursor was observed. In the shock compression data from Barker [38] and the ramp compression data from Smith [11] where a velocity pullback was observed,  $\sigma_E(x)$  represents the precursor peak and

the extent of the (negative) error bar represents the position of the symbol if the minimum pullback velocity was used to calculate  $\sigma_E(x)$ . The errors bars for Gupta [39], Winey [40] and Trivedi [41] are shown as reported. There is a general trend of  $\sigma_E$  decay as a function of distance away from the loading surface ranging from 14.5 GPa at 2  $\mu\text{m}$  to 0.02 GPa at 25mm. Significant scatter in the data is observed within 120 $\mu\text{m}$  from the loading surface where time dependence is expected to be strongest.

The circle and square symbols represent data for ramp and shock loading, respectively. The symbols connected by red lines represent different sample thicknesses with identical stress loading history (taken on the same shot). The samples from the Janus ramp compression experiments, Smith [11] and those of Gupta [39] were prepared using identical source Al and e-beam deposition processes to yield common microstructures and purities. These data sets span sample thicknesses between  $\sim 6$ -200 $\mu\text{m}$ . Within the 26-180  $\mu\text{m}$  data reported by Gupta [39] there is a clear trend of  $\sigma_E$  decay with propagation thickness. However, we note that in the 6-30  $\mu\text{m}$  data reported by Smith [11],  $\sigma_E$  is observed to stay constant or even increase as a function of propagation thickness. As illustrated in Fig. 3(b), under ramp compression, plasticity at  $x=0$  initiates and at a stress level which is a function of the loading strain rate. Away from the loading surface the strain rate increases as a function of  $x$ , due to stress-strain nonlinearity, towards a value consistent with a shock wave rise time [11]. This increase in  $\dot{\epsilon}$  with  $x$  can result in higher values of measured  $\sigma_E(x)$  further away from the loading surface. Near the loading surface, this acts as a competing process to the expected dissipative plastic flow behind the elastic front and is, we suggest, an explanation for why the data of Smith [11] does not decay with propagation thickness. We note that the peak stress in the experiments of Smith [11] and Gupta [39] were 50-200 GPa and 4 GPa, respectively and, as described below the laser experiments by Smith are up to two orders of magnitude higher strain rate.

Also shown as an insert to Fig. 5 is the  $\sigma_E$ - $x$  data for a commonly used alloy of Al: Al 6061-T6. Aluminum 6061-T6 is one of the most widely used of the 6xxx series of silicon-magnesium alloys. Its composition is 96-99% aluminum with 0.8-1.2% magnesium, 0.4-0.8% silicon and other minor constituents [46]. The -T6 designation indicates that the alloy has been solutionized and artificially aged to improve its mechanical properties for structural applications. The T6 hardening treatment varies by manufacturer but usually involves a solution treatment at 810K followed by quenching in water and then aging for a few hours at around 450 K. This process leads to a material with a  $\text{Mg}_2\text{Si}$  precipitate phase evenly distributed inside the grains which act as impediments to dislocation flow. In Fig. 5,  $\sigma_E$  for



Al 6061-T6 increases slowly as function of decreasing propagation thickness [47]. There is a convergence between pure Al and Al 6061-T6 for thinner sample thicknesses (i.e higher strain rates).

Recent studies on pure Al [8], in split-Hopkinson pressure bar (SHPB) experiments, demonstrated a sudden increase in the flow stress above a strain rate of  $\sim 10^3 \text{ s}^{-1}$ . Measurements of the temperature dependence of  $\sigma_E$  at this transition  $\dot{\epsilon}^0$  [8] and at  $\sim 10^6 \text{ s}^{-1}$  (under shock compression) [9] were consistent with phonon drag dislocation flow. In Fig. 6, we plot  $\sigma_E$  versus the strain rate,  $\dot{\epsilon}$ , in aluminum for a range of shock and ramp compression experiments. Only data sets from Fig. 5 where  $u(t)$  profiles were available are represented in Fig. 6. Here, a strong correlation in the instantaneous  $\sigma_E$ - $\dot{\epsilon}$  response is evident from  $\dot{\epsilon} \sim 10^3$ - $10^9 \text{ s}^{-1}$ . The data set taken as a whole represents a large range of initial Al microstructures. The laser ramp compression samples had  $\sim 1 \times 5 \text{ }\mu\text{m}$  grains while the work of Kanel [9] used single crystal samples. A fit to the ramp and shock data in Fig. 6 reveal a power law dependency of the form,

$$\sigma_E = 1.12 \times 10^{-3} (\dot{\epsilon})^{0.43}, \quad (5)$$

which appears relatively independent on the initial sample microstructure. The power law dependence between  $\sigma_E$  and  $\dot{\epsilon}$ , is consistent with an increase in the dislocation saturation density with strain rate [32].

Shown for comparison, as insert to Fig. 6, is the strain rate dependency of Al 6061-T6. Here, dislocations flow through the fcc aluminum matrix readily, but get pinned when they interact with the precipitates. The stress must be increased in order for the dislocations to bow out and break free to propagate further. The critical stress is the Orowan stress, or various generalizations such as in the Friedel-Fleischer model. The process of dislocations breaking free from the nanoscale precipitates is largely an athermal mechanism rather than an activated process [53]; as a result, it is largely rate independent. In the plot of stress versus strain rate, this athermal process leads to a nearly constant stress below some threshold rate. Above the threshold, phonon drag is expected to cause the stress to increase with rate. For  $\dot{\epsilon} < 5 \times 10^6 \text{ s}^{-1}$ ,  $\sigma_E$  for Al 6061-T6 is observed to be relatively insensitive to strain rate suggesting deformation is below the phonon drag threshold. At  $5 \times 10^6 \text{ s}^{-1}$  the response of pure Al and Al 6061-T6 are consistent. A number of studies have been reported recently [11, 54] in which the dynamic yield strength of pure Al has been compared with that of Al 6061-T6 under ramp compression conditions at different strain rates. The data presented in Fig. 6 indicates that reported differences in dynamic strength are likely to be strongly effected by the differences in impurity levels (including alloying) as well strain rate effects.

#### IV. Conclusions

Obtaining quantitative information on time-dependent material response at high strain rates is difficult due to the existence of large gradients in density, which can vary rapidly in time (several ns) and space (several  $\mu\text{s}$ ). Experimentally the challenges are two fold: (1) Develop an experimental technique to generate high strain rate conditions, (2) Develop capabilities to diagnose time-dependent material response. The most common technique for generating compressive strain rates  $< \sim 10^6 \text{ s}^{-1}$  have been through plate impact experiments on mm-thick samples. Here the material is shock-loaded at a fixed strain rate of  $\sim 10^9 \text{ s}^{-1}$  which drops as a function of propagation distance towards a finite steady-wave rise-time determined by time-dependent material response. The primary diagnostic for these experiments velocimetry in which the interfacial velocity history is recorded after the stress wave has traversed the sample. The result is a space- and time- integrated measurement of material response at a well-defined propagation distance. For a common drive, measurement of peak elastic stress versus propagation distance is then typically fit with phenomenological dislocation kinetics models to obtain information on time-dependent plasticity. These models are, in turn, derived from observations under quasi-static conditions. As the sample thicknesses used in flyer-plate experiments are typically  $\sim \text{mm}$  in scale the measured strain rates are in the  $\sim 10^3\text{-}10^6 \text{ s}^{-1}$  range (Fig. 4). Other techniques used infer high- $\dot{\epsilon}$  dislocation flow employ x-ray diffraction during shock compression [57] and high resolution imaging of recovered shock compressed samples [58]. Atomistically high- $\dot{\epsilon}$  plasticity ( $> \sim 10^9 \text{ s}^{-1}$ ) has been explored through molecular dynamics (MD) simulations where empirical information may then be used to develop analytical expressions for use within continuum modeling [32] (multi-scale modeling approach). Measurements within the  $\sim 10^6\text{-}10^9 \text{ s}^{-1}$  strain rate range are needed to bridge the gap between traditional experimental techniques and ultra-high strain rate atomistic calculations. In this paper we presented data on bcc Fe and fcc Al in which the dependencies of strongly time-dependent plastic flow are measured across a strain rate range of  $10^6\text{-}10^8 \text{ s}^{-1}$ . We use a recently developed laser ramp wave loading technique to compress 6-70  $\mu\text{m}$  thick samples while systematically varying the loading strain rate [17].

The  $\sigma_E\text{-}\dot{\epsilon}$  response of a material at a distance  $x'$  from the loading surface is a convolution of the instantaneous material response and the integrated time-dependent response from  $x=0 \rightarrow x'$ . In SHPB experiments on fcc metals, Cu and Al, it was found that the instantaneous strain rate was dominant over the strain rate history in determining the sudden rise of stress at high strain rates

characteristic of phonon drag dislocation flow. Indeed, in the analysis of VISAR traces from our data we find that, independent of sample thickness, there exists a strong correlation between instantaneous values of  $\sigma_E$  and  $\dot{\epsilon}$ ; for both ramp and shock loading. For Fe we observe an increase in the peak elastic stress at  $\dot{\epsilon} > \sim 2 \times 10^6 \text{ s}^{-1}$  and  $\sigma_E \sim 1.3 \text{ GPa}$  which is consistent with a transition to phonon drag dislocation flow. In fcc Al, within the phonon drag regime, our data reveal a power law dependence of  $\sigma_E$  with  $(\dot{\epsilon})^{0.43}$  which is consistent with an increase in the saturation density with increasing strain rate. The laser ramp data presented here represent some of the highest strain rates achieved within the laboratory.

This work was performed under the auspices of the U.S. Dept. of Energy by Lawrence Livermore National Laboratory under Contract DE-AC52-07NA27344. The authors wish to thank J.R. Asay, Y.M. Gupta, J.M. Winey, P.B. Trivedi and H. Huang for providing VISAR velocity data, which were included in the figures.

## Appendix A

In order to investigate how the elastic precursor is related to the kinetics of plastic flow, we have applied a rate-dependent, dislocation-based continuum model of plasticity (Fig 3(b)). This model relates the shear stress (strength) to dislocation mobilities and work hardening. A dislocation mobility law gives the velocity of dislocation motion to the shear stress [55]. In some cases such mobility curves have been calculated from first principles using molecular dynamics. Work hardening is the increase in strength due to entanglement of dislocations, and the strength is taken to increase as the square root of the dislocation density in a form due to Taylor [22]. The dislocation density evolves with the plastic flow through multiplication and annihilation. For sufficiently high dislocation densities, multiplication and annihilation cancel and the dislocation density comes to a steady state that has been termed saturation. This kind of model with explicit dislocation evolution is a generalization of the Gilman model [56].

Specifically, we use a mechanical threshold stress (MTS) form [53] developed recently for a multiscale model of the strength of tantalum [5]. The parameters for tantalum were derived from first principles through a multiscale hierarchy starting with density functional theory quantum mechanical calculations of bonding, and then progressing through classical molecular dynamics calculations of

dislocation mobilities and dislocation dynamics calculations of multiplication, saturation, and dislocation type partitioning (parameterized through an Orowan factor). That multiscale sequence has not been undertaken for iron at this point. It is a major, multi-year effort to do so. Instead, we have taken the parameters for the body-centered cubic metal tantalum and scaled them for the body-centered cubic metal iron. Such a scaling is not expected to be quantitatively precise, but it should be qualitatively correct. It provides insight into the precursor dynamics.

The model is fully specified by the following relations [5, 35]. The von Mises shear stress (strength)  $\sigma_e$  is the sum of work hardening and mobility contributions:

$$\sigma_e = M \left[ (\tau_\alpha + \hat{\tau}) + \tau^* \tau_p \right] \quad (6)$$

where  $M$  is a Taylor factor that accounts for the orientation distribution (texture) of the polycrystal grains,  $\tau_\alpha$  is an athermal stress,  $\tau_p$  is the Peierls stress and  $\tau^*$  is the relative dislocation mobility. The mobility is comprised of thermal activation and phonon drag contributions:

$$\tau^* = \left( \tilde{\tau}_{\text{Therm}}^5 + \tilde{\tau}_{\text{Drag}}^5 \right)^{1/5} \quad (7)$$

$$\tilde{\tau}_{\text{Therm}} = \alpha_0 e^{T/\alpha_i} \left[ \left( \frac{v}{c_0} + \tilde{v}_0 \right)^{\gamma(T)} - (\tilde{v}_0)^{\gamma(T)} \right] \quad (8)$$

$$\gamma(T) = \beta_0 + T/\beta_T \quad (9)$$

$$\tilde{\tau}_{\text{Drag}} = \chi_0 \left[ \left( \frac{v}{c_0} \right) - \chi_1 \right] \left[ 1 - \left( \frac{v}{c_0} \right)^2 \right]^{-1/2} \quad (10)$$

where  $v$  is the dislocation velocity,  $c_0$  is the shear wave velocity and  $T$  is the temperature. The other quantities are parameters listed in Table 1. The work hardening is of the form

$$\hat{\tau} = \beta b G \sqrt{\rho} \quad (11)$$

where  $G$  is the shear modulus and  $\beta$  is a parameter. The plastic strain rate is given by Orowan's Law

$$\dot{\epsilon}^p = \eta \rho b v / M \quad (12)$$

where  $\rho$  is the dislocation density,  $b$  is the Burgers vector length (the nearest neighbor interatomic spacing) and  $\eta$  is the Orowan factor accounting for partitioning of plastic flow between different kinds of dislocations. The dislocation density evolves as the material is deformed according to:

$$\dot{\rho} = R \left( 1 - \frac{\rho}{\rho_{\text{Sat}}} \right) \dot{\epsilon}^p \quad (13)$$

where  $R$  is the dislocation multiplication rate and  $\rho_{\text{sat}}$  is the saturation dislocation density. The saturation density is taken to be a function of the strain rate:

$$\rho_{\text{sat}} = \rho_{0s} \left( \frac{\dot{\gamma}}{\dot{\gamma}_N} + S_0 \right)^n \quad (14)$$

where apart from the saturation density and the plastic strain rate all of the quantities in this formula are parameters. The only pressure dependence in the model enters through the Peierls stress, which is taken to be a polynomial of the pressure. The parameters in the models for tantalum and vanadium have been derived from first principles, as explained above, and are published in Ref. [5]. The parameters for iron are not available in the literature, so we scale the tantalum parameters using dimensional analysis in the following way. The parameters  $\alpha_t$  and  $\beta_t$  have dimensions of temperature, and are assumed to scale with the melt temperature. The parameters  $\tau_\alpha$  and  $\tau_p$  include dimensions of stress and are assumed to scale with the shear modulus. The parameters  $b$ ,  $\rho_{0s}$ , and  $R$  have dimensions that are the length scale to different powers and that length scale is taken to be the lattice constant. The parameter  $\dot{\gamma}_N$  has a dimension of  $\text{time}^{-1}$  and is assumed to scale with  $b/c_0$ . The parameters for iron are given in Table 1, as inferred from the parameters for tantalum and these scaling relations.

$b$	2.485 Å	$M$	3.07
$\tau_\alpha$	20 MPa	$G(P = 0)$	90.4 GPa
$\tau_p$	688 MPa	$\eta$	2.0
$c_0$	3875 m/s	$\rho_{0s}$	$1.5 \times 10^{11} / \text{m}^2$
$\tilde{\nu}_0$	$10^{-9}$	$\dot{\epsilon}_N$	$2.23 \text{ s}^{-1}$
$\alpha_0$	2.3643	$S_0$	650
$\alpha_t$	623 K	$n$	0.59
$\beta_0$	0.2757	$R$	$1.3 \times 10^{17} / \text{m}^2$
$\beta_t$	1409 K	$\beta$	0.4
$\chi_0$	37.166	$\chi_1$	0.03075

**Table 1. Parameters used in time-dependent plasticity model for Fe.**

## References:

- [1] J.N. Johnson, O.E. Jones and T.E. Michaels, J. Appl. Phys. **41** 2330 (1970).
- [2] Y.M. Gupta, J. Appl. Phys. **48**, 5067 (1978).
- [3] J.R. Asay, G.R. Fowles, G.E. Duvall, M.H. Miles, R.F. Tinder, J. Appl. Phys. **43**, 2132 (1972).
- [4] H.-S. Park, K. T. Lorenz, R. M. Cavallo, S. M. Pollaine, S. T. Prsbrey, R. E. Rudd, R. C. Becker, J.V. Bernier, B.A. Remington, Phys. Rev. Letts. **104**, 135504 (2010).
- [5] N.R. Barton, J.V. Bernier, R. Becker, A. Arsenlis, R. Cavallo, J. Marian, M. Rhee, H.-S. Park, B. Remington, and R.T. Olson, J. Appl. Phys. **109**, 073501 (2011).
- [6] A.M. Lennon, K.T. Ramesh, Inter. J. Plas. **20**, 269 (2004).
- [7] K.E. Duprey and R.J. Clifton, AIP **505**, 447 (1999).
- [8] K. Sakino, J. Phys. IV **10**, Pr9-58 (2000).
- [9] G.I. Kanel, S.V. Razorenov, K. Baumung, J. Singer, J. Appl. Phys. **90**, 136 (2001).
- [10] R.F. Smith, J. H. Eggert, M. D. Saculla, A. F. Jankowski, M. Bastea, D. G. Hicks, G.W. Collins, Phys. Rev. Letts. **101**, 065701 (2008).
- [11] R.F. Smith, J.H. Eggert, A.F. Jankowski, P.M. Celliers, M.J. Edwards, Y.M. Gupta, J.R. Asay, G.W. Collins, Phys. Rev. Lett. **98**, 065701 (2007).
- [12] P.M. Celliers, D.K. Bradley, G.W. Collins, D.G. Hicks, T.R. Boehly, W.J. Armstrong, Rev. Sci. Instrum. **75**, 4916 (2004).
- [13] R.F. Smith, S.M. Pollaine, S.J. Moon, K.T. Lorenz, P.M. Celliers, J.H. Eggert, H-S Park, G.W. Collins, Phys. Plas. **14**, 057105 (2007).
- [14] O.V. Fat'yanov, R. L. Webb, and Y. M. Gupta, J. Appl. Phys. **97**, 123529 (2005).
- [15] B.J. Jensen, G.T. Gray III and R.S. Hixson, J. Appl. Phys. **105**, 103502 (2009).
- [16] W. Arnold, Dynamisches Werkstoffverhalten von Armco-Eisen bei Stosswellenbelastung (VDI-Verlag, Duesseldorf, 1992);
- [17] J.E. Eggert, private communications.  $C_L$  calculated from ramp compression data taken on Armco-Fe on the Sandia Z machine.
- [18] B.J. Jensen, P.A. Rigg, M.D. Knudson, R.S. Hixson, G.T. Gray III, B.H. Sencer, F.J. Cherne, in Shock Compression of Condensed Matter, p. 232, 2005. Edited by M.D. Furnish, M. Elert, T.P. Russell, and C.T. White.
- [19] R.W. Armstrong, W. Arnold and F.J. Zerilli, J. Appl. Phys. **105**, 1 (2009).
- [20] L.M. Barker and R.E. Hollenbach, J. Appl. Phys. **45**, 4872 (1974); L.M. Barker, J. Appl. Phys. **46**, 2544 (1975).
- [21] P.L. Hérel, J. Phys. Colloq. **C3**, 77 (1988).
- [22] J.W. Taylor, J. Appl. Phys. **36**, 3146 (1965).
- [23] J.N. Johnson and R.W. Rohde, J. Appl. Phys. **42**, 4171 (1971).
- [24] D. Bancroft, E.L. Peterson, and S. Minshell, J. Appl. Phys. **27**, 291 (1956).
- [25] T. de Resseguier and M. Hallouin, J. Appl. Phys. **84**, 1932 (1998).
- [26] A.G. Ivanov, S. A. Novikov, and V. A. Sinitsyn, Sov. Phys. Solid State **5**, 196 (1963).
- [27] Z. Rosenburg, A. Erez and Y. Parton, J. Phys. E **16**, 198 (1983).

- [28] J.W. Swegle and D.E. Grady, J. Appl. Phys. **58**, 692 (1985).
- [29] D.E. Grady, J. Appl. Phys. **107**, 013506 (2010).
- [30] Sir G. Taylor, "Propagation and decay of blast waves" in The scientific papers of Sir Geoffrey Ingram Taylor – Collected Works, (Edited by G.K. Batchelor) Vol. 3, pp. 221-235. Cambridge University Press, England (1963).
- [31] G.E. Duvall, Iranian Journal of Science and Technology **7**, 57 (1978).
- [32] R. Becker, A. Arsenlis, G. Hommes, J. Marian, M. Rhee, L. H. Yang, LLNL-TR-417075 (2009).
- [33] R.W. Klopp, R.J. Clifton and T.G. Shawki, Mech. Mat. **4**, 375 (1985).
- [34] In an elastic medium the shear stress,  $\tau$ , (one-half the von Mises equivalent deviatoric stress) may be related to  $\sigma_x$  by,  $\tau = \frac{1-2\nu}{2(1-\nu)}\sigma_x$ , where the Poisson ratio  $\nu$  for Fe is 0.288, which gives  $\tau = 0.298\sigma_x$ . For uniaxial strain in a plastically deforming material the rate of plastic shear strain,  $\dot{\gamma}$ , may be related to the longitudinal strain rate by the following relationship,  $\dot{\gamma} \approx \frac{3}{4}\dot{\epsilon}$ . This assumes that the elastic shear strain rate is zero; i.e. that hardening effects due to strain (dislocation density) and strain rate are negligible.
- [35] B.A. Remington, P. Allen, E.M. Branga, J. Hawreliak, D. Ho, K.T. Lorenz, H. Lorenzana, J.M. McNaney, M.A. Meyers, S. W. Pollaine, K. Rosolankova, B. Sadik, M. S. Schneider, D. Swift, J. Wark and B. Yaakobi, Mat. Sci. Tech. **22**, 474 (2006).
- [36]
- [37] M. Bastea, S. Bastea and R. Becker, Appl. Phys. Letts. **95**, 241911 (2009).
- [38] L.M. Barker, B.M. Butcher, and C.H. Karnes, J. Appl. Phys. **37**, 1989 (1966).
- [39] Y.M. Gupta, J.M. Winey, P.B. Trivedi, B.M. LaLone, R.F. Smith, J.H. Eggert, and G.W. Collins, J. Appl. Phys. **105**, 036107 (2009).
- [40] J.M. Winey, B.M. LaLone, P.B. Trivedi, and Y.M. Gupta, J. Appl. Phys. **106**, 073508 (2009).
- [41] P.B. Trivedi, J.R. Asay, Y.M. Gupta, and D.P. Field, J. Appl. Phys. **102**, 083513 (2007).
- [42] B.M. Butcher and D.E. Munson, in Dislocation Dynamics, edited by A. R. Rosenfield, G. T. Hahn, A. L. Bement, Jr., and R. I. Jaffe (McGraw-Hill, New York, 1968).
- [43] V.H. Whitley, S.D. McGrane, D.E. Eakins, C.A. Bolme, D.S. Moore, J. F. Bingert, J. Appl. Phys. **109**, 013505 (2011)
- [44] T.E. Arvidsson, Y.M. Gupta and G.E. Duvall, J. Appl. Phys. **46**, 4474 (1975).
- [45] C.H. Karnes, in Mechanical Behavior of Materials under Dynamic Loads, edited by U.S. Lindholm (Springer-Verlag, New York, 1968).
- [46] Alcoa 6061 data sheet
- [47] B. Banerjee and A.S. Bhawalkar, J. Mech. Mat. Str. **3**, 391 (2008).
- [48] J.-P. Davis, J. Appl. Phys. **99**, 103512 (2006).
- [49] J.N. Johnson and L. M. Barker, J. Appl. Phys. **40**, 4321 (1969).
- [50] J.R. Asay, private communications.
- [51] J. Lipkin and J.R. Asay, J. Appl. Phys. **48**, 182 (1977).
- [52] K. Sakino, J. Phys. IV **134**, 183 (2006).
- [53] A. Argon, Strengthening Mechanisms in Crystal Plasticity (Oxford Univ. Press, Oxford, 2008), Section 6.2.
- [54] T.J. Volger, T. Ao, J.R. Asay, Int. J. Plas. **25**, 671 (2009).
- [55] J. P. Hirth and J. Lothe, *Theory of Dislocations*, 2<sup>nd</sup> ed. (Krieger, Malabar, Florida, 1982).
- [56] J. J. Gilman, J. Appl. Phys. **36**, 2772 (1965).
- [57] Hawreliak, Laue diffraction of Cu foils.
- [58] M. Meyers et al....

Smith et al. – Fig. 1

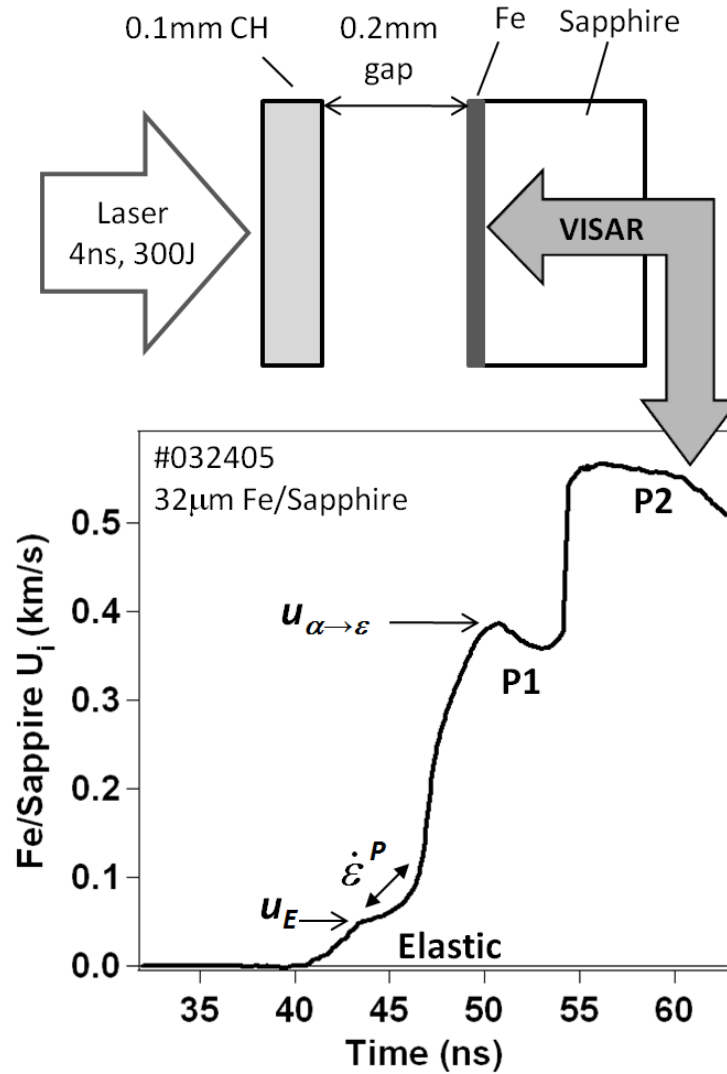


Fig. 1. Experimental setup for laser-driven ramp compression of an Fe foil. The VISAR records the emergence of a three wave structure at the Fe/sapphire interface: an Elastic Wave, a plastic wave (P1) with a peak stress associated with the onset of the  $\alpha \rightarrow \epsilon$  phase transformation and a subsequent plastic wave (P2) within which transformation to the  $\epsilon$ -phase occurs.  $\dot{\epsilon}^P$  is the strain rate at the initial onset of plasticity and is found to be strongly correlated to the peak elastic precursor velocity,  $u_E$ . In our analysis  $\dot{\epsilon}^P$  is defined over the velocity interval  $u_E \rightarrow 2u_E$ .



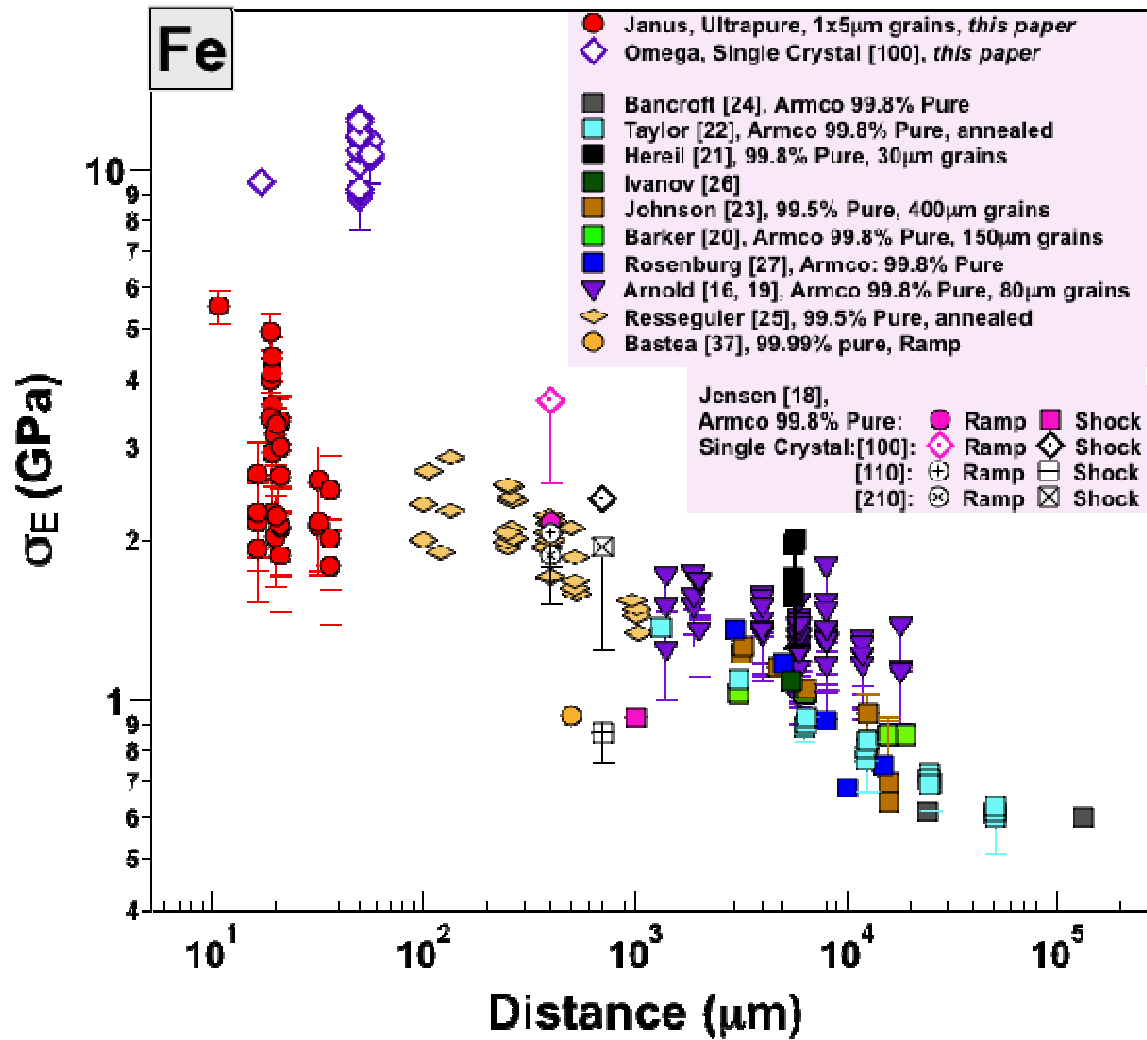
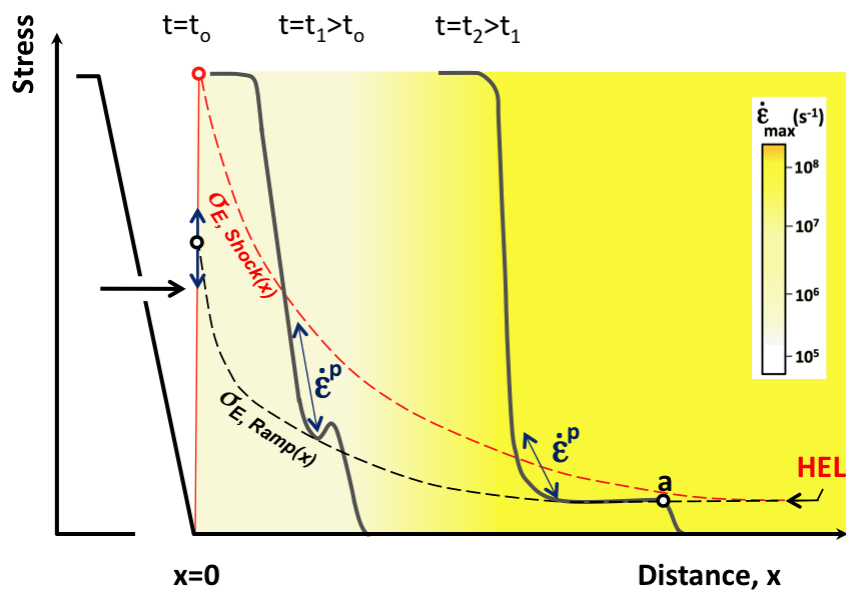


Fig. 2.  $\sigma_E$  as a function of propagation distance from the loading surface for Fe. The red circles and purple open diamond symbols represent the laser driven ramp compression data on polycrystalline and single crystal [100] Fe samples, respectively.

Smith et al. – Fig. 3

(a)



(b)

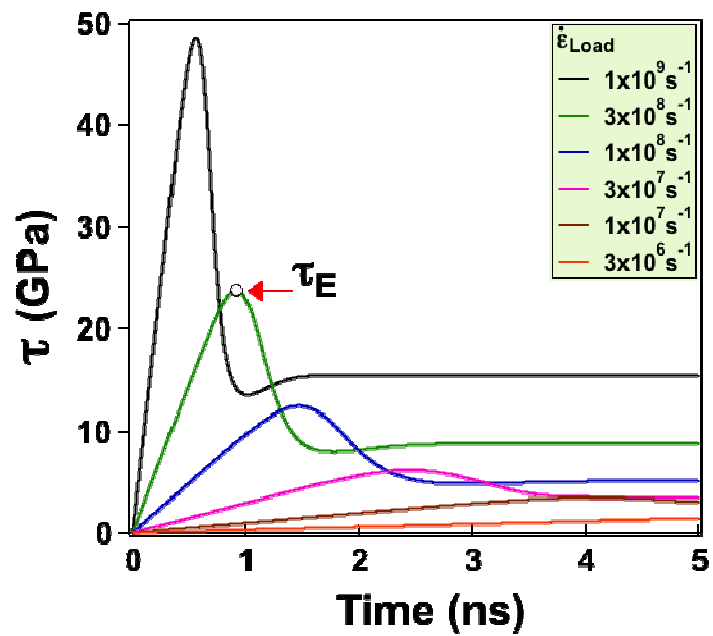


Fig. 3(a) Ramp wave evolution at different times during compression.  $\dot{\epsilon}$  is the strain rate at the initial onset of plasticity and is found to be strongly correlated to  $\sigma_E$ . In our analysis  $\dot{\epsilon}$  is defined over the velocity interval  $u_E \rightarrow 2u_E$ . The color scale illustrates how, in contrast to shock loading, for ramp compression  $\dot{\epsilon}_{\max}$  increases as a function of distance from the loading surface. (b) Calculated shear stress as a function of time at the loading surface for an Fe sample assuming a linear ramp compression with loading strain rates,  $\dot{\epsilon}_{\text{Load}}$ .  $\tau_E$  represents the stress at the onset of inelastic deformation and is shown to be a function of  $\dot{\epsilon}_{\text{Load}}$ .

Smith et al. – Fig. 4

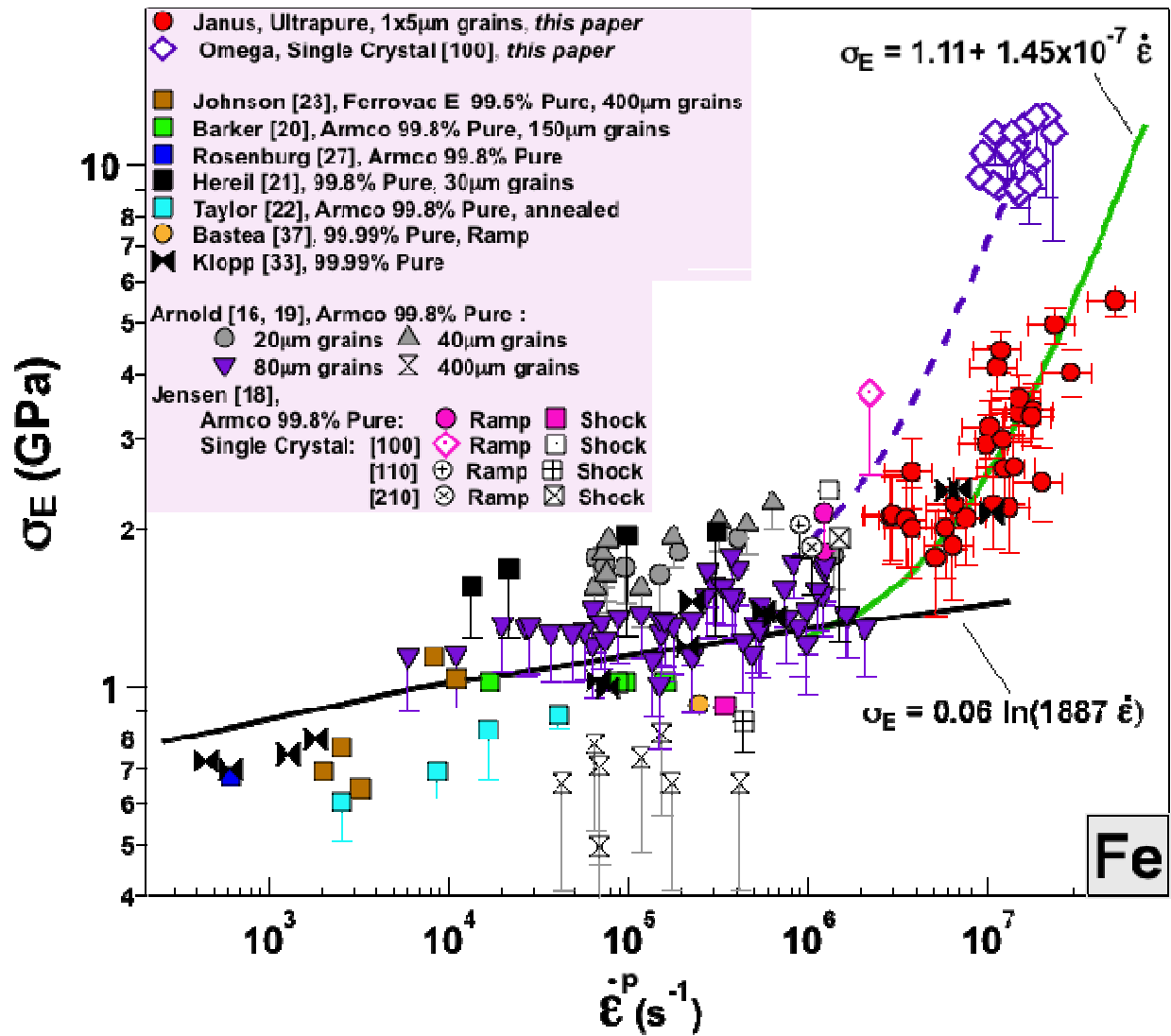


Fig. 4. Peak Elastic stress,  $\sigma_E$ , plotted against the strain rate of initial plastic deformation,  $\dot{\epsilon}^p$  for Fe. The sudden increase of  $\sigma_E$  at high  $\dot{\epsilon}^p$  is consistent with the onset of phonon drag mediated plastic flow for  $\sigma_E > \sim 1.3$  GPa and  $\dot{\epsilon}^p > \sim 2 \times 10^6$  s<sup>-1</sup>. Single crystal [100] samples are shown as the open diamond symbols. Here, the more limited data set suggests an equivalent transition to a phonon drag regime at  $\sim 10^6$  s<sup>-1</sup> but offset to higher levels of  $\sigma_E$ .

Smith et al. – Fig. 5

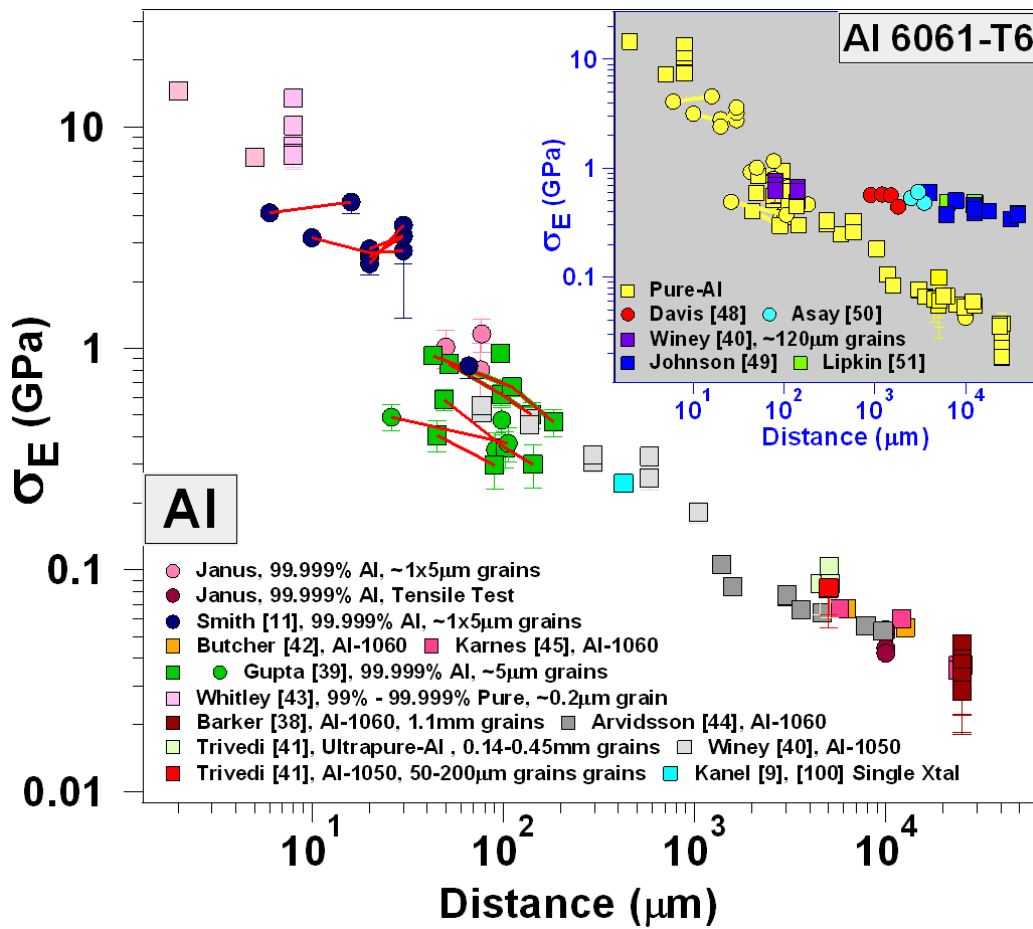
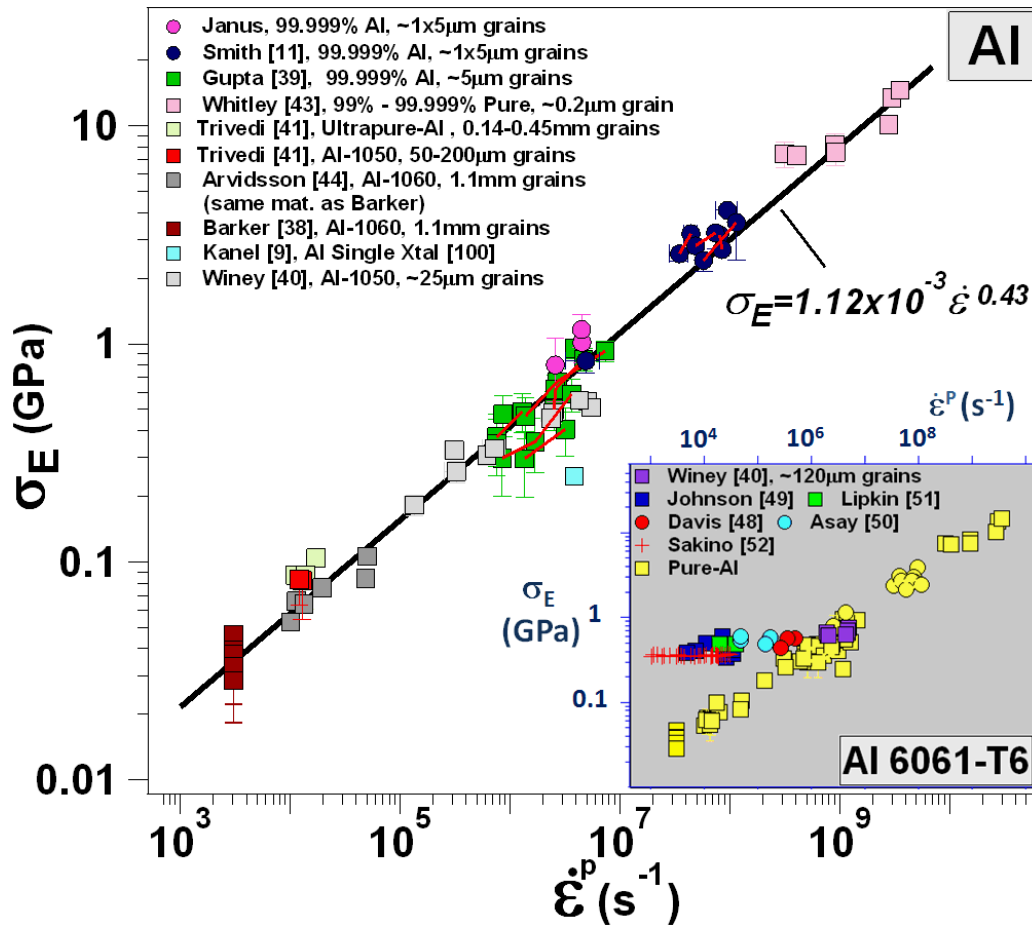


Fig. 5.  $\sigma_E$  versus distance for >99.9% pure-Al. The circles represent ramp compression experiments while the squares represent shock compression. The symbols connected by red lines signify different thickness with common loading conditions (same shot). Also shown are tensile bar test on the same Al microstructure as used in the laser ramp experiments and in the data of Smith [11] and Gupta [39]. Insert shows  $\sigma_E$ - $\dot{\epsilon}$  data for Al 6061-T6.

Smith et al. – Fig. 6



**Fig. 6. Peak elastic stress,  $\sigma_E$ , plotted against the strain rate of initial plastic deformation,  $\dot{\epsilon}$ , for pure Al. Insert shows  $\sigma_E$ - $\dot{\epsilon}$  data for Al 6061-T6.**